

**Original citation:**

Song, Tzu-Hsi, Sanchez Silva, Victor, Eldaly, Hesham and Rajpoot, Nasir M. (Nasir Mahmood). (2017) Dual-channel active contour model for megakaryocytic cell segmentation in bone marrow trephine histology images. IEEE Transactions on Biomedical Engineering

**Permanent WRAP URL:**

<http://wrap.warwick.ac.uk/87312>

**Copyright and reuse:**

The Warwick Research Archive Portal (WRAP) makes this work by researchers of the University of Warwick available open access under the following conditions. Copyright © and all moral rights to the version of the paper presented here belong to the individual author(s) and/or other copyright owners. To the extent reasonable and practicable the material made available in WRAP has been checked for eligibility before being made available.

Copies of full items can be used for personal research or study, educational, or not-for profit purposes without prior permission or charge. Provided that the authors, title and full bibliographic details are credited, a hyperlink and/or URL is given for the original metadata page and the content is not changed in any way.

**Publisher's statement:**

"© 2017 IEEE. Personal use of this material is permitted. Permission from IEEE must be obtained for all other uses, in any current or future media, including reprinting /republishing this material for advertising or promotional purposes, creating new collective works, for resale or redistribution to servers or lists, or reuse of any copyrighted component of this work in other works."

**A note on versions:**

The version presented here may differ from the published version or, version of record, if you wish to cite this item you are advised to consult the publisher's version. Please see the 'permanent WRAP URL' above for details on accessing the published version and note that access may require a subscription.

For more information, please contact the WRAP Team at: [wrap@warwick.ac.uk](mailto:wrap@warwick.ac.uk)

# Dual-Channel Active Contour Model for Megakaryocytic Cell Segmentation in Bone Marrow Trepine Histology Images

Tzu-Hsi Song, Victor Sanchez, *Member, IEEE*, Hesham EIDaly, and Nasir M. Rajpoot, *Senior Member, IEEE*

**Abstract**—Assessment of morphological features of megakaryocytes (special kind of cells) in bone marrow trephine biopsies play an important role in the classification of different subtypes of Philadelphia-chromosome-negative myeloproliferative neoplasms (Ph-negative MPNs). In order to aid hematopathologists in the study of megakaryocytes, we propose a novel framework that can efficiently delineate the nuclei and cytoplasm of these cells in digitized images of bone marrow trephine biopsies. The framework first employs a supervised machine learning approach that utilizes color and texture features to delineate megakaryocytic nuclei. It then employs a novel dual-channel active contour model to delineate the boundary of megakaryocytic cytoplasm by using different deconvolved stain channels. Compared to other recent models, the proposed framework achieves accurate results for both megakaryocytic nuclear and cytoplasmic delineation.

**Index Terms**—Megakaryocyte segmentation, Digital pathology, Bone marrow trephine biopsies, Active contours.

## I. INTRODUCTION

**M**YELOPROLIFERATIVE neoplasms (MPNs) are neoplastic disorders of bone marrow hematopoietic stem cells, in which the hematopoietic cells proliferate abnormally. Philadelphia-chromosome-negative (Ph-negative) MPNs, one of pathological subgroups of MPNs, mainly comprise polycythemia vera (PV), essential thrombocythemia (ET) and primary myelofibrosis (PMF). For PV, ET and PMF, the annual incidence rates ranges from 0.01 to 2.61, 0.21 to 2.27, and 0.22 to 0.99 per 100,000 population, respectively [1]. These Ph-negative MPN diseases exhibit a varied but partially overlapping set of clinical and cytomorphological features. This inevitably makes the task of objectively classifying a bone marrow trephine biopsy sample into one of the above Ph-negative MPN diseases quite challenging in some cases [2]–[7]. In order to create a standard set of pathologic measurements that aid in distinguishing the three diseases of Ph-negative MPNs in routine clinical diagnosis, the World Health Organization (WHO) has established a set of diagnostic guidelines to associate clinical diagnostic data with

observed histological and cytological features and molecular-genetic findings [4]–[7]. The present guidelines clearly show that morphological features play a key role in diagnosis and classification. This, however, may cause low reproducibility of diagnostic results and inter-observer variability among hematopathologists [5], [6]. In an attempt to resolve these challenges, computer-assisted diagnosis (CAD) techniques can be introduced to assist pathologists in classifying the different subtypes of Ph-negative MPNs efficiently and objectively by using digital pathology images [8], [9]. Here, trephine histology is used to help in the identification of these bone marrow diseases with CAD techniques. Trepine histology examination is one of the bone marrow examinations and suitable for representing core bone marrow biopsy specimens. Trepine histology allows a complete assessment of bone marrow structure and of the pattern of distribution of any abnormal infiltrate [2], [3], [5]. The staining protocol used in trephine histology, namely Hematoxylin and Eosin (H&E) staining, is a fairly standard protocol used worldwide.

Within the context of CAD using bone marrow trephine biopsy images, a reliable measurement in the diagnosis of bone marrow diseases is the morphology of megakaryocytes (MKs), which constitute a population of bone marrow resident cells that are responsible for the production of blood platelets [4]–[7]. Compared to other bone marrow cells, MKs usually have distinctive morphological features, like large-sized nuclei and more well-defined cytoplasmic region (see Fig. 1). It is thus of particular interest to perform a quantitative analysis of the morphological features of MKs through the detection of the corresponding nucleus and delineation of the cytoplasmic boundary. However, unlike the nucleus, the cytoplasm of MKs is often partially occluded by nearby cells, other cytoplasm and other types of tissue, as shown in Fig. 1. Moreover, the corresponding cytoplasmic boundary usually comprises weak edges (See Fig. 1.(c)). All these aspects make the task of delineating MKs quite challenging.

Image segmentation approaches based on deformable models, such as level set methods, have been widely used to successfully delineate various structures in pathology images [10]–[14] and widely applied for tissue and nucleus segmentation for cancer diagnosis, such as breast cancer [11]–[13], [15]–[17] and prostate cancer [18], [19]. In a more general context, region-based level set methods [20]–[24] have been particularly successful by incorporating region-based statistical information into an energy functional. Unlike edge-based level set methods, which use image gradients, region-

Manuscript received April 19, 2016; reviewed October 26, 2016; accepted March 25, 2017.

T.H. Song is with the Department of Computer Science, University of Warwick, UK email: T.H.Song@warwick.ac.uk.

V. Sanchez is with the Department of Computer Science, University of Warwick, UK email: V.F.Sanchez-Silva@warwick.ac.uk.

H. EIDaly is with Haematology Oncology Diagnostic Service, Addenbrookes Hospital, Cambridge, UK email: hesham.eldaly@addenbrookes.nhs.uk.

N.M. Rajpoot is with the Department of Computer Science, University of Warwick, UK email: Nasir.Rajpoot@ieee.org.

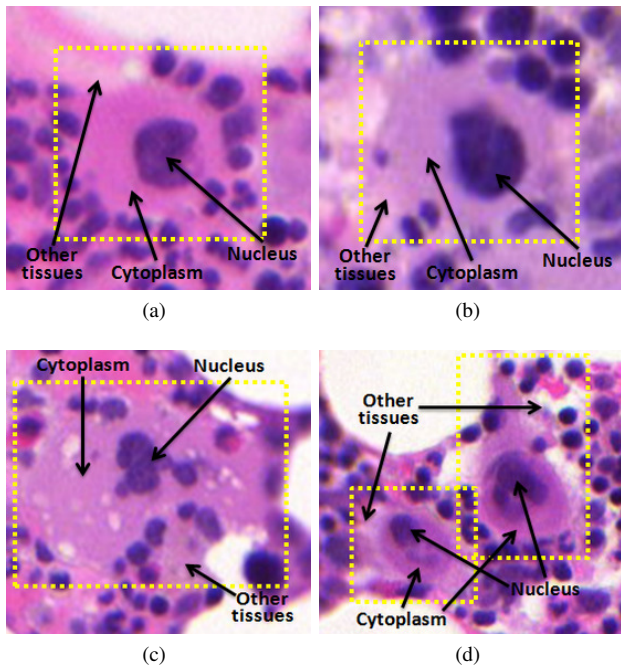


Fig. 1. Representative examples of bone marrow trephine histology images. The MKs are contained within yellow rectangles. Note that the MK cytoplasm is often partially occluded by nearby cells, other cytoplasmic and non-smooth regions, and their boundaries usually comprise weak edges.

based methods use the global region information to stabilize their responses to local variations. These methods can attain a higher segmentation accuracy than edge-based level set methods on images with weak boundaries. Among the state-of-the-art level set methods, the Chan-Vese (CV) model [20], [21], [25], [26] is one of the most representative and efficient ones. This particular model assumes that the image statistics in two regions remain relatively constant; these two regions are the inside and outside of the evolving contour. The CV model, therefore, performs very well on images where these two regions are relatively smooth. However, this model often leads to poor segmentation results for non-smooth images, i.e., with intensity inhomogeneities, due to the fact that the deformation movement of the evolving curve is guided by global region information [26]–[31].

Many improvements have been proposed to solve some of the limitations of the CV model [21], [25]–[35]. In [31], Li *et al.* propose an efficient region-based level set method by introducing a local binary fitting (LBF) energy term, which enables the extraction of local information with a Gaussian kernel and can be used on images with intensity inhomogeneities. Wang *et al.* [32] introduce the Local Chan-Vese (LCV) model, which employs both global image information and local statistics for efficiently segmenting images with intensity inhomogeneities. In [33], Zhou *et al.* combine a local active contour model and an adaptive diffusion flow active contour model to improve medical segmentation in inhomogeneous regions with weak edges. In order to control the movement of the evolving contour towards the object’s boundary in images with intensity inhomogeneities, Ji *et al.* propose a fitting energy functional that minimizes a local likelihood energy term derived from the

image intensity within each pixel’s neighborhood [34]. Brown *et al.* propose a multi-phase active contour model for global multiple region segmentation [36]. Although all these methods improve segmentation accuracy of the CV model on images with weak edges and intensity inhomogeneities, they are all sensitive to the position of the initial contour and the value of parameters [32], [35], [37], [38].

Within the context of cell segmentation in pathology images, most of the recently proposed methods focus on nuclei segmentation as cytoplasm segmentation remains a challenging task in many types of tissue images [10], [13], [14], [39]. For instance, Ali *et al.* propose an adaptive active contour model with shape prior for nuclear segmentation in prostate cancer tissue [40]. Among the very few methods that are capable of segmenting nuclear and cytoplasmic regions, the one proposed by Nosrati *et al.* [41] uses color features of manually labelled regions to generate a prior feature response map. This map is used along with containment and exclusion energy terms to simultaneously segment multiple regions [41].

In bone marrow trephine biopsy images, a very limited number of approaches have been proposed for the specific case of MKs. The method proposed by Ballaro *et al.* [42], [43] is one of the most representatives. In their work, the authors propose an unsupervised image analysis framework to detect and delineate the nuclear and cytoplasmic regions of MKs by using morphological operations, pyramid functions and shape detection [42], [43]. Their framework, however, requires that a single MK be located in the center of the image to be analyzed and be surrounded by a smooth region. In the majority of bone marrow trephine biopsy images, MKs are usually surrounded by non-smooth regions depicting other types of cells and non-MK cytoplasmic regions.

In this paper, we propose a framework for delineation of MK nuclear and cytoplasmic boundaries based on a novel region-based level set model. Our proposed framework first employs color and texture features of different stain color channels of the image in a supervised machine learning setting to delineate MK nuclei. It then employs a novel region-based active contour model, formulated as a level set function, to delineate the corresponding cytoplasmic boundaries. Under the assumption that MK nuclei are usually surrounded by cytoplasm, our proposed model incorporates the difference in intensity between internal and external regions of the evolving contour across two deconvolved stain channels into an energy functional to delineate the cytoplasmic boundary. We refer to this novel model as a dual-channel active contour (DCAC) model. Extensive experiments with a large dataset objectively compare the performance of the proposed model with other state-of-the-art methods. Specially, we compare our framework using a two-fold approach. First we evaluate the delineation accuracy of MK nuclei against other supervised and unsupervised methods. Second, we evaluate the accuracy of our DCAC model in segmenting the corresponding cytoplasmic regions against the CV model, the LBF model, our previously proposed circumscribing active contour (CAC) model [44], and the multi-region active contour model in [41]. We show that our framework is capable of delineating MKs very accurately. We particularly show that the DCAC

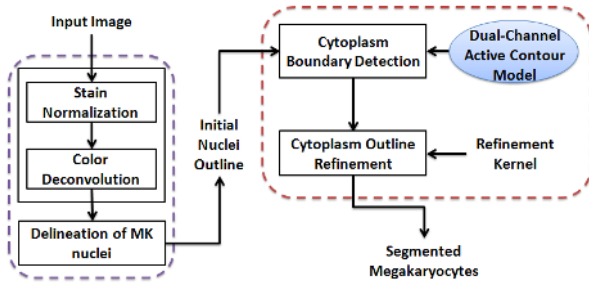


Fig. 2. The workflow of the framework with our proposed DCAC model.

model can identify the MK cytoplasmic boundaries with high accuracy even in challenging cases where the MK cytoplasm has weak edges and is surrounded by non-smooth regions.

The rest of this paper is organized as follows. Section II introduces the proposed framework for nuclear and cytoplasmic boundary delineation and describes the proposed DCAC model in detail. In Section III, we present and discuss the experimental results and comparison with other methods. Finally, we draw conclusions in Section IV.

## II. THE PROPOSED FRAMEWORK

Fig. 2 graphically illustrates the steps involved in the proposed framework to delineate MK nuclei and cytoplasm. The steps within the purple dashed box correspond to pre-processing and MK nuclei delineation. The delineation of cytoplasmic boundaries is performed by the steps within the red dotted box. The initial contour used by our proposed DCAC model is the boundary of the corresponding MK nucleus. All these steps are described in detail in this section.

### A. Stain Normalization and Color Deconvolution

Bone marrow trephine biopsy slides are commonly dyed using the standard Hematoxylin and Eosin (H&E) stains. Color constancy in these images might be affected by variations on the microscopy light levels, chemical coloring reactivity and staining procedures. These factors may influence the image processing methods used to identify cellular structures. In order to minimize any negative effects on the delineation of MKs, input images are first processed by stain normalization and stain deconvolution. Stain normalization standardizes the stain color while stain deconvolution separates the image into a number of channels that correspond to the stain used. The latter allows analyzing each stain, or channel, separately. We employ a non-linear mapping approach, which estimates stable stain matrices by using an image-specific color descriptor and a robust color classification framework for a particular stain, with channel statistics for stain normalization by using a source image, as proposed in [45]. For color deconvolution, we employ the stain color descriptor method in [45] to separate the H&E stained images into two color channel images. The H-channel image provides information about the positions of the MK nuclei, while the E-channel image emphasizes other tissue constituents, including the MK cytoplasm. An example of the output generated by the stain normalization and color

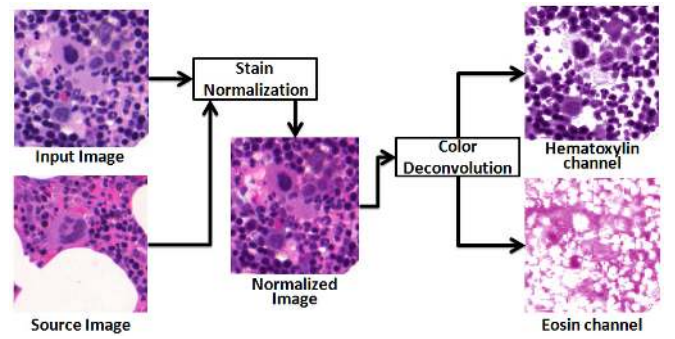


Fig. 3. Example results of stain normalization and color deconvolution process. Input images are in the left, while output stain channel images are in the right.

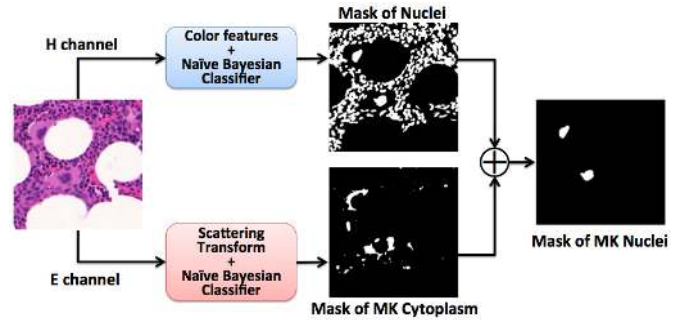


Fig. 4. Example intermediate results of the process followed to identify MK nuclei. The masks of all nuclei and MK cytoplasm are used to identify MK nuclei.

deconvolution process is shown in Fig. 3. We can observe that indeed, the H- and E-channel images provide clear information about the regions depicting MK nuclei and MK cytoplasm, respectively.

### B. Delineation of MK Nuclei

After obtaining the two stain channel images, we employ a machine-learning based approach to identify MK nuclei. We first crop several small patches (10X10 pixels) from different training H-channel images. There is no overlap between adjacent patches as no sliding window is used. These training patches depict MK nuclear regions, MK cytoplasmic regions, other cytoplasmic regions and the background region, e.g., fat tissue. We then use a Naive Bayesian classifier with color features extracted from these H-channel training patches to generate a binary mask of all nuclei. It is important to note that MK nuclei are similar in color and texture to other nuclei, thus the obtained mask depicts all possible nuclei in the image. In order to distinguish MK nuclei from other nuclei in the nuclei mask, we also generate a binary mask depicting MK cytoplasm. To this end, we apply the scattering transform [46] on E-channel training images to extract texture features of MK cytoplasm. These features are used in another Naive Bayesian classifier along with color features to generate the cytoplasm mask. Since the MKs have larger cytoplasmic regions than other cells, we overlap these two masks and measure the area surrounding each nucleus that overlaps a cytoplasmic region in order to identify MK nuclei. In other words, we are

interested in identifying those nuclei surrounded by a large cytoplasm. Fig. 4 shows example intermediate results of the process followed to identify MK nuclei. We delineate the boundaries of the detected nuclei and further refine them using a simple region-based active contour model. Specifically, we use the CV model, since MK nuclei are usually smooth dark regions surrounded by another relatively smooth region, i.e. the cytoplasm. The CV model includes four energy terms: length, area, internal region intensities and external region intensities. The energy functional is then as follows:

$$\begin{aligned}
F(c_1, c_2, C) &= \mu \text{Length}(C) + \nu \text{Area}(\text{inside}(C)) \\
&+ \lambda_1 \int_{\text{inside}(C)} |I(x, y) - c_1|^2 dx dy \\
&+ \lambda_2 \int_{\text{outside}(C)} |I(x, y) - c_2|^2 dx dy
\end{aligned} \quad (1)$$

where  $C$  denotes the evolving contour,  $c_1$  and  $c_2$  are, respectively, the average intensity of the regions inside and outside of  $C$ ;  $I(x, y)$  denotes the pixel intensity in the image at position  $(x, y)$ , and  $\mu$ ,  $\nu$ ,  $\lambda_1$  and  $\lambda_2$  are constant parameters. The last two energy terms in (1) are the internal and external region intensity terms, respectively. These two terms are usually called the external energy because they generate an energy force from the image and not the contour itself. These terms control the contour's movement externally. The evolving contour  $C$  can be represented by the level-set function  $\phi(x, y)$  [20], [21], where  $\phi(x, y) > 0$  if the position  $(x, y)$  is inside of  $C$  and  $\phi(x, y) < 0$  if the position  $(x, y)$  is outside of  $C$ . If position  $(x, y)$  lies on  $C$ ,  $\phi(x, y) = 0$ . Let us define the evolving curve  $C$  in the image domain  $\Omega$ . The energy functional  $F(c_1, c_2, C)$  can then be formulated in terms of the level-set function  $\phi(x, y)$  as follows:

$$\begin{aligned}
F(c_1, c_2, \phi) &= \mu \int_{\Omega} \delta(\phi(x, y)) |\nabla \phi(x, y)| dx dy \\
&+ \nu \int_{\Omega} H(\phi(x, y)) dx dy \\
&+ \lambda_1 \int_{\Omega} |I(x, y) - c_1|^2 H(\phi(x, y)) dx dy \\
&+ \lambda_2 \int_{\Omega} |I(x, y) - c_2|^2 H(1 - \phi(x, y)) dx dy
\end{aligned} \quad (2)$$

where the Heaviside function  $H(z)$ , Dirac delta function  $\delta(z)$ ,  $c_1$  and  $c_2$  are:

$$H(z) = \begin{cases} 1, & \text{if } z \geq 0 \\ 0, & \text{if } z < 0 \end{cases} \quad (3)$$

$$\delta(z) = \frac{d}{dz} H(z) \quad (4)$$

$$c_1 = \frac{\int_{\Omega} I(x, y) H(\phi(x, y)) dx dy}{\int_{\Omega} H(\phi(x, y)) dx dy} \quad (5)$$

$$c_2 = \frac{\int_{\Omega} I(x, y) H(1 - \phi(x, y)) dx dy}{\int_{\Omega} H(1 - \phi(x, y)) dx dy}. \quad (6)$$

The refined nuclear boundary generated by employing the model in (2) serves as the initial contour for our proposed

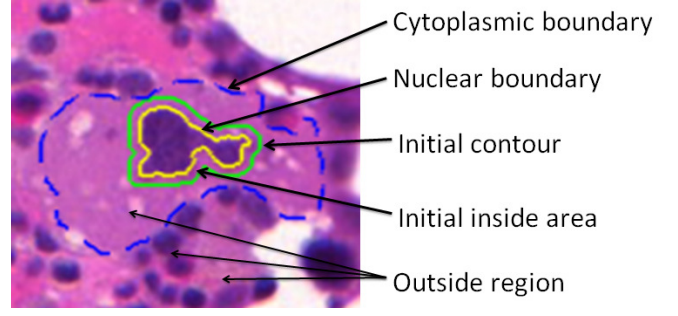


Fig. 5. An example initial contour and the corresponding inside region and the nuclear boundary,  $C_n$ . The initial contour (in green) is obtained by dilating  $C_n$  (in yellow).

DCAC model, which we use to delineate the corresponding MK cytoplasm boundary.

### C. The Proposed DCAC Model

1) *Proposed external energy force:* As explained in Section I, MK cytoplasm is usually a relatively smooth region partially occluded by other tissues and surrounded by non-smooth regions. Based on this observation, our proposed DCAC model considers intensity information of both the H- and E-channel images to delineate the boundary of MK cytoplasm. Similar to the CV model, our DCAC model also employs four energy terms: length, area, internal region intensities and external region intensities. It employs as the initial contour, the corresponding previously delineated nuclear boundary. Our DCAC model, however, uses as the inside region of the evolving contour  $C$ , the region inside of  $C$  excluding the nucleus. Therefore, the initial contour is dilated by a small amount in order to define the initial region inside of  $C$ . We denote the previously delineated nuclear boundary in terms of a level-set function as  $C_n = \{(x, y) \mid \phi_n(x, y) = 0\}$ . The proposed inside region intensity term,  $F_{in}$ , in our DCAC model is then given by:

$$\begin{aligned}
F_{in}(c'_1, \phi) &= \int_{\text{inside}(C) - \text{inside}(C_n)} |I(x, y) - c'_1|^2 dx dy \\
&= \int_{\Omega} |I(x, y) - c'_1|^2 \left( \widehat{H}(\phi(x, y), \phi_n(x, y)) \right) dx dy
\end{aligned} \quad (7)$$

where the function  $\widehat{H}(a, b)$  is defined as the difference of two Heaviside functions:

$$\widehat{H}(a, b) = H(a) - H(b) \quad (8)$$

and the inside mean value  $c'_1$  is defined as:

$$c'_1 = \frac{\int_{\Omega} I(x, y) \widehat{H}(\phi(x, y), \phi_n(x, y)) dx dy}{\int_{\Omega} \widehat{H}(\phi(x, y), \phi_n(x, y)) dx dy} \quad (9)$$

The energy function in (7) assumes a relatively smooth region, which is true as long as the inside region of  $C$  represents exclusively the cytoplasm. Under this assumption, the energy term in (7) is then minimized when the inside region of  $C$  exclusively comprises the MK cytoplasm. An example initial contour and the corresponding inside region and  $C_n$  are depicted in Fig. 5.

It is worth recalling that the outside region intensity term of the CV model in (2) is expected to be minimized when the pixels intensities in the outside region are similar to the value  $c_2$  (see (1)). In our DCAC model, we assume that the outside region is non-smooth and, therefore, several pixels in this outside region are likely to be dissimilar to the value of  $c_2$ . However, we expect that when the contour is located in the cytoplasmic boundary, the pixels in the outside region are sufficiently different from the mean of the inside region, i.e.  $c'_1$  in (9). In other words, we expect that the integral  $\int_{outside(C)} (I(x,y) - c'_1)^2$  results in a large value when the contour is located at the cytoplasmic boundary. Based on this observation, we use this large difference between pixels in the inside region of  $C$  (i.e., those depicting the MK cytoplasm) and those in the outside region of  $C$  to be the outside region intensity term. To this end, we introduce a maximum intensity difference value,  $MD$ , in the outside region intensity term to help the contour to expand and accurately detect the cytoplasmic boundary:

$$MD = \max\{|I(x,y) - c'_1|\} \quad (10)$$

The proposed outside region intensity term in our model is then given as follows:

$$F_{out}(c'_1, \phi, MD) = \int_{\Omega} |MD - |I(x,y) - c'_1||^2 \times (1 - H(\phi(x,y))) dx dy \quad (11)$$

According to (11),  $F_{out}$  is expected to be minimized when the difference between pixels in the region outside of  $C$  and  $c'_1$  is sufficiently large and close to  $MD$ . Therefore,  $MD$  represents the maximum difference between a pixel in the region outside of  $C$  and  $c'_1$ , under the assumption that the outside region of the evolving contour is non-smooth, which is the case when detecting MK cytoplasm in bone marrow trephine biopsies. The proposed external energy force in our model is then defined as follows:

$$F_{ex}(c'_1, \phi, MD) = \lambda_1 \int_{\Omega} |I(x,y) - c'_1|^2 \times \left( \widehat{H}(\phi(x,y), \phi_n(x,y)) \right) dx dy + \lambda_2 \int_{\Omega} |MD - |I(x,y) - c'_1||^2 \times \left( 1 - H(\phi(x,y)) \right) dx dy \quad (12)$$

## 2) Proposed external energy force on stain channel images:

In order to improve the delineation accuracy of the cytoplasmic boundary using the external energy force in (12), we employ intensity information from the two stain channel images. As we discussed earlier, the H-channel image usually shows the position of nuclei very clearly while the E-channel image is usually useful to discriminate between cytoplasm and other

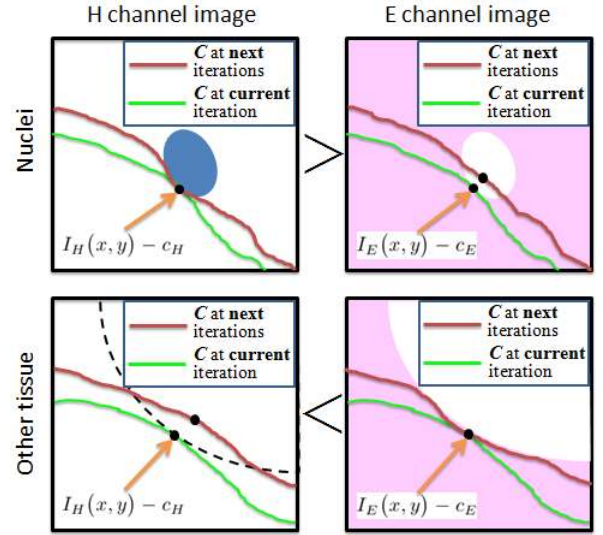


Fig. 6. The upper row shows how the difference between pixel values and  $c_H$  is larger on the H-channel image than on the E-channel image. This helps to stop the evolving contour when encountering other nuclei outside the cytoplasmic regions. The bottom row shows how the E-channel image can be used to efficiently distinguish between the MK cytoplasmic region and other tissues, different from nuclei.

tissues. We take advantage of this and define the external force in (12) for each of these two channel images:

$$F_{ex\_H}(c'_H, \phi, MD) = \lambda_1 \int_{\Omega} |I_H(x,y) - c'_H|^2 \times \left( \widehat{H}(\phi(x,y), \phi_n(x,y)) \right) dx dy + \lambda_2 \int_{\Omega} |MD_H - |I_H(x,y) - c'_H||^2 \times \left( 1 - H(\phi(x,y)) \right) dx dy \quad (13)$$

$$F_{ex\_E}(c'_E, \phi, MD) = \lambda_1 \int_{\Omega} |I_E(x,y) - c'_E|^2 \times \left( \widehat{H}(\phi(x,y), \phi_n(x,y)) \right) dx dy + \lambda_2 \int_{\Omega} |MD_E - |I_E(x,y) - c'_E||^2 \times \left( 1 - H(\phi(x,y)) \right) dx dy \quad (14)$$

where  $c'_H$  and  $c'_E$  are the average intensity values of the inside regions of  $C$  in the H-channel image, denoted by  $I_H(x,y)$ , and E-channel image, denoted by  $I_E(x,y)$ , respectively.  $MD_H$  and  $MD_E$  denote the MD values for the H- and E-channel images, respectively. Fig. 6 illustrates how the H- and E-channel images can help the evolving contour to detect the extent of the MK cytoplasmic region. In order to accurately differentiate MK cytoplasmic regions from other non-MK cytoplasmic regions, we use either the external energy force in (13) or in (14) based on the channel that provides the most discriminative information. To this end, we define a

binary weight  $W$  as follows:

$$W(c'_H, c'_E) = \begin{cases} 1, & \text{if } |I_H(x, y) - c'_H| \geq |I_E(x, y) - c'_E| \\ 0, & \text{otherwise} \end{cases} \quad (15)$$

The binary weight  $W$  considers the difference between pixels and the mean intensity of the region inside of  $C$  in each stain channel image. We use this binary weight to select the stain channel image that provides the largest difference. This is based on the observation that the H- and E-channel images provide distinct boundary information. The H-channel image emphasizes the nuclear boundaries more strongly than the E-channel image. On the other hand, the E-channel image emphasizes the cytoplasmic boundaries more strongly than H-channel image. This allows us to accurately control the contour's expansion towards the MK cytoplasmic boundary and accurately minimize the external energy term. It is important to note that if  $W$  is defined as a weight that can take any value in the range  $[0, 1]$ , the result would again mix the information provided by the H- and E-channel images, thus defeating the purpose of channel deconvolution. Combining the external energy forces as defined for the two stain channel images with binary weight  $W(c'_H, c'_E)$ , our external energy force is then given as follows:

$$F_{ex\_total} = W(c'_H, c'_E)F_{ex\_H} + (1 - W(c'_H, c'_E))F_{ex\_E} \quad (16)$$

In order to prevent over-segmentation of non-MK cytoplasmic regions in the outside region of  $C$ , we restrain the contour's expansion to those pixels located in a ring-like region surrounding  $C$ . The boundary of this ring-like region is given by:

$$\phi_\gamma(x, y) = \phi(x + \gamma\vec{\eta}_x, y + \gamma\vec{\eta}_y) \quad (17)$$

$$\vec{\eta}(x, y) = \frac{\nabla\phi(x, y)}{|\nabla\phi(x, y)|} \quad (18)$$

where the parameter  $\gamma$  controls the width of the ring-like region and  $\vec{\eta}(x, y)$  denotes the normal vector of the expanding contour. An example of this ring-like region is shown in Fig. 7. The complete set of forces in our DCAC model is then as follows:

$$\begin{aligned} F_{total} = & \mu \int_{\Omega} \delta(\phi(x, y)) |\nabla\phi(x, y)| dx dy \\ & + \nu \int_{\Omega} H(\phi(x, y)) dx dy \\ & + F_{ex\_total} \hat{H}(\phi_\gamma(x, y), \phi(x, y)) \end{aligned} \quad (19)$$

It is important to note that the ring-like expansion,  $\phi_\gamma$ , in conjunction with  $F_{ex\_total}$  play key roles to help the contour to efficiently and accurately conform to the cytoplasmic boundary. It is also important to note that if the contour encapsulates smooth cytoplasm from neighbouring cells, and not only the smooth cytoplasm from the MK to be delineated,  $F_{out}$  in (11) may still be a valid force making the contour evolve. In this case, the internal energy terms in (19) help prevent these types of leakages.

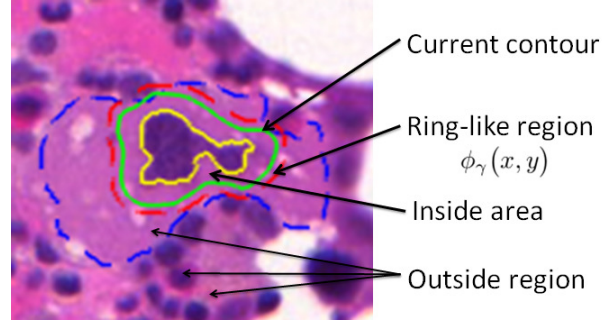


Fig. 7. An example evolving contour and the corresponding ring-like region. The green contour denotes the evolving contour  $C$ ; the blue dashed contour denotes the cytoplasmic boundary; the yellow contour denotes the nuclear boundary,  $C_n$ ; and the red dashed contour denotes the ring-like region boundary.

The energy functional in (19) can be minimized with respect to  $\phi$  by deducing the associated Euler-Lagrange equation for  $\phi$  as follows:

$$\begin{aligned} \frac{\partial\phi}{\partial t} = & \delta(\phi) \left\{ \text{div} \left( \frac{\nabla\phi}{|\nabla\phi|} \right) - \nu - (\delta(\phi_\gamma) - \delta(\phi)) \times \right. \\ & \left[ W(c'_H, c'_E) \left( \lambda_1 (I_H - c'_H)^2 \right. \right. \\ & \quad \left. \left. - \lambda_2 (MD_H - |I_H - c'_H|)^2 \right) \right. \\ & \left. + (1 - W(c'_H, c'_E)) \left( \lambda_1 (I_E - c'_E)^2 \right. \right. \\ & \quad \left. \left. - \lambda_2 (MD_E - |I_E - c'_E|)^2 \right) \right] \left. \right\} \quad (20) \end{aligned}$$

where  $\text{div}(\cdot)$  is the divergence operator. The contour's expansion is terminated if the following criterion is met:

$$\begin{aligned} & \frac{1}{\int \mathbf{1}(F_{total}^j(x, y) > T) dx dy} \times \\ & \left( \left| \int_{\phi^j > 0} F_{total}^j \mathbf{1}(F_{total}^j(x, y) > T) dx dy \right. \right. \\ & \left. \left. - \int_{\phi^{j-1} > 0} F_{total}^{j-1} \mathbf{1}(F_{total}^j(x, y) > T) dx dy \right| \right) < \tau \left( \alpha \sqrt{\frac{\gamma}{5}} \right)^2 \end{aligned} \quad (21)$$

where  $\tau$  is the time step,  $\phi^j$  denotes the  $j$ th iteration of the evolving curve,  $F_{total}^j$  is the total energy in the  $j$ th iteration,  $F_{total}(x, y)$  is the total energy at the pixel  $(x, y)$ ,  $\mathbf{1}(x)$  is the indicator function and  $T$  is a threshold value to discard those pixels that feature very low energy values. In this work, we set the stop parameter  $\alpha$  to 0.06 and the threshold value  $T$  to 0.5 based on several experiments. These values guarantee that the total energy difference between two consecutive iterations is minimal. Finally, after the cytoplasmic boundary is delineated using our DCAC model, we use the cubic spline interpolation with Gaussian smoothing as the refinement kernel [47] to smooth its shape.

### III. RESULTS AND DISCUSSION

Three sets of experiments were performed. The first set evaluates the accuracy of MK nuclei detection as described

TABLE I  
MK NUCLEI DETECTION ACCURACY OF THREE EVALUATED METHODS

Framework	Precision	Recall	F1-score
Ballaro's method [42], [43]	0.84	0.5	0.6269
Supervised framework of CAC [44]	0.7	0.875	0.7758
Proposed MK nuclei detection method	<b>0.86</b>	<b>0.833</b>	<b>0.8518</b>

in Section II-B. The second set evaluates the performance of our DCAC active contour model to delineate MK cytoplasmic boundaries as compared to other region-based level-set methods. The third set evaluates our complete framework against the multi-region active contour in [41], which allows delineating the nuclear and cytoplasmic boundaries simultaneously. All results are obtained using 50 digitized images of bone marrow trephine biopsies digitized at  $40\times$  magnification objective using the Omnyx VL120 digital slides scanner installed at the University Hospital Coventry and Warwickshire (UHCW), UK.

#### A. Evaluation of MK nuclei detection

We compare our MK nuclei detection method with an automatic unsupervised MK detection framework [42], [43], which we implement in Matlab, and the supervised MK nuclei detection method previously proposed in [44], which uses an Adaboost classifier to generate the cytoplasm mask. We use 50 bone marrow trephine images, including 73 megakaryocytes, of early-stage ET and PMF diseases in this evaluation; 50% of the images are used for training and 50% for testing. Table I tabulates results in terms of precision, recall and accuracy for the three methods. Precision is the percentage of selected MK nuclei that are correct and Recall gives the percentage of correct MK nuclei that are selected. The F1-score is the harmonic mean of Precision and Recall and is computed as  $2 \times Precision \times Recall / (Precision + Recall)$ . Results in Table I are computed using manually annotated ground truth provided by a junior pathology trainee and a senior pathologist (H. EIDaly) from Addenbrookes Hospital, UK.

Our MK selection method provides an accuracy of 85%, attaining the best performance. It is important to emphasize that the automatic unsupervised framework (Ballaro's method) in [42], [43] is limited to identify the MK that is closest to the center of the input image. Therefore, this framework can only identify one MK nucleus per image. If the MK is located far from the image center with several other large overlapping structures, that framework is likely to obtain an incorrect result. Our MK nuclei detection method, on the other hand, is capable of identifying several MK nuclei regardless of their position in the image. Although our previous supervised framework can provide good accuracy in identifying MK nuclei, the Adaboost classifier requires long times to process the texture of cytoplasm. The proposed method in this work can identify MK nuclei more efficiently with shorter computational times.

#### B. Evaluation of the Proposed DCAC Model

As explained in Section II-B, we expand the delineated nuclear boundary and use this as the initial contour for our

TABLE II  
PARAMETERS OF THE EVALUATED MODELS

AC models	Parameters								
	$\mu$	$\nu$	$\lambda_1$	$\lambda_2$	$\lambda_3$	$\lambda_4$	$\sigma$	$d$	$\gamma$
CV [20]	0.2	0	1	1	—	—	—	—	—
LBF [31]	0.2	0	1	1	—	—	3	—	—
CAC [44]	0.2	0	1.5	1	1.5	1	—	—	—
Multi-region model [41]	—	—	2/0.25	1.05/0.6	—	—	—	10/10	—
Proposed DCAC model	0.2	0	1	1	—	—	—	—	5

DCAC model. The delineated nuclear boundary is dilated by 3 pixels. This guarantees that the inside region of initial contour includes cytoplasm. For this evaluation, we use 40 MK cases in 30 images. Manually annotated ground truth data depicting MK nuclear and cytoplasmic boundaries are provided by a junior trainee and a senior pathologist. Fig. 8 shows four sample visual results obtained by our DCAC model. Note that the identified cytoplasmic boundaries cover most of the ground truth cytoplasmic region.

We compare our proposed DCAC model with Ballaro's method [42], [43], and the CV, the LBF, and the CAC models. These last three models are all region-based level-set methods. For all evaluated models, we use the same initial contour and post-processing to delineate and refine the shape of the MK cytoplasmic boundaries. In order to provide a fair comparison, the parameters of the region-based level-set methods are set to those values that provide the best performance on the MK dataset (see Table II). For the CAC model,  $\lambda_3$  and  $\lambda_4$  denote the parameters of internal and external texture energy forces, respectively. The local region in the LBF model is generated using the Gaussian kernel with  $\sigma = 3$ . In our DCAC model, we set the width of the ring-like region to  $\gamma = 5$  pixels. The ring-like region should be wide enough to provide enough information to compute the external energy force. Empirical evaluations on our test images show that a width of  $\gamma = 5$  pixels provides a high delineation accuracy.

The time step  $\tau$  is set to 0.99 for all evaluated models. We use up to five hundred iterations. It is important to mention that all evaluated models, except for the LBF model, have a criterion to stop the evolution process [20], [31]. Fig. 9 shows visual results of the four models for four MKs in different images, as compared to the ground truth. Note that the proposed DCAC model visually attains a better performance than the other three models, particularly when the MK is surrounded by a non-smooth region. According to Fig. 9, the CV and LBF models fail to detect the cytoplasmic boundary as the evolving contour does not achieve convergence and shrinks back to the original contour. Let us recall that the CV model attempts to minimize the difference between the energy associated with the internal and external regions of the evolving contour. However, if the external region is non-smooth, the corresponding force may cause the contour to shrink back to the initial contour. The LBF model considers the local region surrounding the evolving contour to reduce any negative effects associated with non-smooth regions. However, our results show that the evolving contour of the LBF model also shrinks back to the initial contour (see Fig. 9). This is mainly due to the fact that the inside region of the evolving contour includes the highly smooth nuclear region, and there-



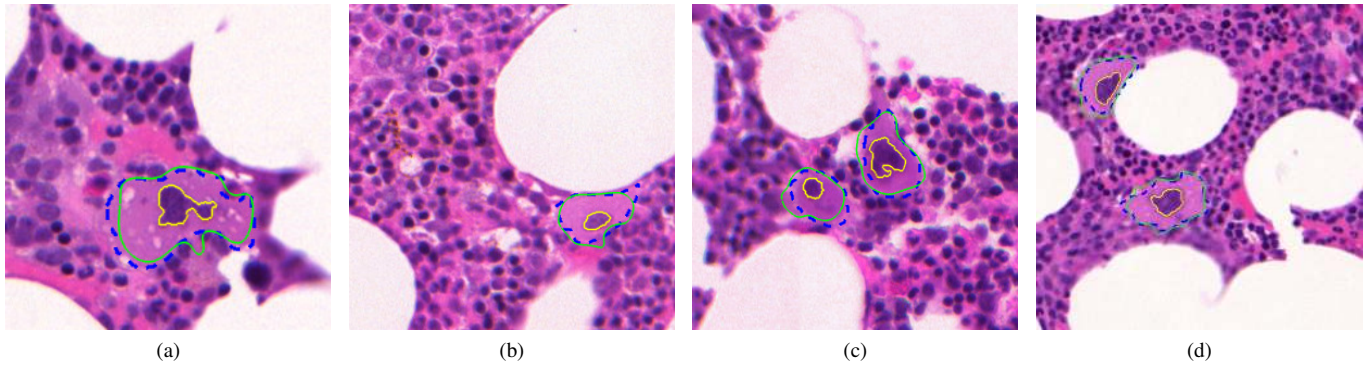


Fig. 8. Visual results of our proposed DCAC model for identification of MK cytoplasmic boundaries. Yellow contours denote the segmented nuclear boundaries by the CV model. This boundary is used as the initial contours in the proposed model after dilating them. Green contours denote the identified cytoplasmic boundaries. Blue dashed contours denote the ground truth as manually annotated.

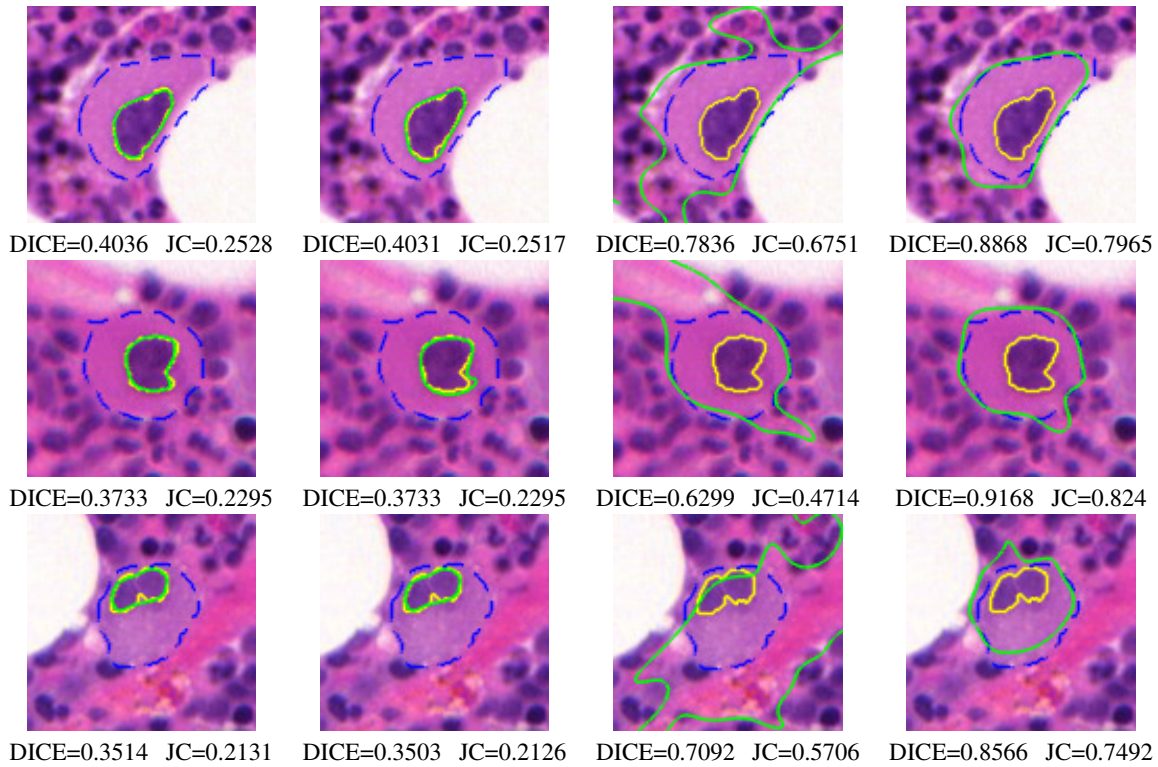


Fig. 9. Visual results of CV model (first column), LBF model (second column), CAC model (third column) and DCAC model (fourth column). The yellow line denotes the initial contour; the green line denotes the final result and the blue dashed line denotes the ground truth.

fore, the energy term associated with the outside region is overwhelmed by the inside region force, forcing the contour to shrink back. Note that although the CAC model is capable of expanding the evolving contour towards the cytoplasmic boundary, it results in over-segmentation due to the difficulty of converging within the non-smooth region surrounding the MK cytoplasm and the similarity in intensities between the MK cytoplasm and other tissues surrounding it.

To quantitatively evaluate the performance of these four models, we use the Dice similarity coefficient (DICE) and the Jaccard coefficient (JC), which measure the similarity between the ground truth and the delineated areas. DICE and JC values are zero for the worst delineation results and one for perfect delineation. Table III tabulates the average, minimum

and maximum DICE and JC values for all test images. Note that our DCAC model provides a better performance than that attained by Ballaro's method, mainly because their method uses morphological processing steps which may not be suitable for segmenting inhomogeneous or non-smooth regions. Table III also tabulates the average number of iterations and average computational time at which each model achieves convergence according to their stop criterion. We can see that our DCAC model attains better performance than the other three evaluated models, with average DICE and JC values of 0.8509 and 0.73, respectively. As expected, the CV and LBF models obtain similarly low average DICE and JC values (0.3599 and 0.2328, respectively) because their evolving contours tend to shrink back to the initial contour when the outside region surrounding

TABLE III  
ACCURACY OF BALLARO'S METHOD AND FOUR EVALUATED ACTIVE  
CONTOUR MODELS FOR DELINEATING MKS

AC models		Avg	Std	Min	Max	Iteration	Time(s)
Ballaro's method [42], [43]	DICE	0.5266	0.1383	0.3355	0.7679	—	—
	JC	0.369	0.1337	0.2015	0.6232	—	—
CV [20]	DICE	0.3599	0.1354	0.0394	0.7237	452.1	54.5
	JC	0.2328	0.1625	0.0201	0.5671		
LBF [31]	DICE	0.3583	0.1348	0.0394	0.7218	500	61.2
	JC	0.2312	0.1618	0.0201	0.5658		
CAC [44]	DICE	0.6482	0.1178	0.5215	0.8215	383.6	48.7
	JC	0.5215	0.1481	0.3862	0.6972		
Proposed model	DICE	<b>0.8509</b>	0.0715	0.6712	0.9437	<b>187.3</b>	<b>24.4</b>
	JC	<b>0.73</b>	0.0938	0.557	0.8947		

the cytoplasm is non-smooth, as previously discussed. This table also shows that the average number of iterations and computational time required by our DCAC model is lower than that required by the other evaluated models. This shows that the forces employed by our model can help the evolving contour to quickly reach the desired boundary and achieve convergence.

It is important to recall that our DCAC model employs the ring-like region to reduce any negative effects of the non-smooth regions surrounding the MK cytoplasm on the contour's expansion. This idea is similar to the narrow-band active contour model in [48], [49], with the main difference being that we only consider the outside ring-like region to restrict the external energy force. Although this ring-like region efficiently prevents over-segmentation, there may still be leakages as the proposed model uses global features obtained from the deconvolved stain channels, which may still depict cytoplasmic regions with weak edges. Local information, such as gradient value or orientation, will be introduced to improve the DCAC model [50]. This part of our further work.

### C. Comparison of complete framework with Multi-Region Active Contour Model

We also compare our entire proposed framework with the multi-region active contour model in [41] using the images and ground truth used in the second experiment. The multi-region active contour model allows delineating the nuclear and cytoplasmic boundaries simultaneously. Since the parameters in this model should be manually set for each image, we use a set of optimal parameters that provide the best performance for all our test images. The values of these parameters are tabulated in Table II. We use the same post-processing to smooth the shape of detected MK cytoplasmic boundary in both evaluated methods. Fig. 10 shows visual results of the two methods for five MKs in different images.

We also employ DICE and JC to quantify the accuracy of our entire framework and the multi-region active contour model in delineating MKs, including nuclear and cytoplasmic regions individually. These quantitative results are tabulated in Table IV. According to Table IV and Fig. 10, both models can obtain very similar results for cell delineation, but our framework provides better performance for the case of individual nucleus and cytoplasm delineation. The accuracy level attained by the multi-region model for nucleus delineation may be due to the fact that this model simultaneously segments two regions by calculating the geometrical constraint energy terms for each

TABLE IV  
SEGMENTATION ACCURACY OF THE PROPOSED FRAMEWORK AND THE  
MULTI-REGION ACTIVE CONTOUR MODEL FOR MK CELL, NUCLEAR AND  
CYTOPLASMIC REGIONS

Active contour models		Cell	Nuclei	Cytoplasm
Multi-region model [41]	DICE	0.8706±0.0339	0.7103±0.1902	0.7485±0.0822
	JC	0.7542±0.0821	0.5676±0.1776	0.586±0.1017
Proposed DCAC model	DICE	<b>0.8829±0.03</b>	<b>0.9599±0.0452</b>	<b>0.8557±0.0448</b>
	JC	<b>0.7836±0.0569</b>	<b>0.9262±0.0799</b>	<b>0.7417±0.0681</b>

region, which result in one contour's movement affecting to the other's. In other words, this model favours similar shapes for both contours. It is important to mention that in [41], the authors also propose a model that does not favour similar shapes (i.e., it is oblivious to the shapes). This model may improve the accuracy of nucleus and cytoplasm delineation, especially if these regions are delineated by strong edges. Our framework delineates nuclear and cytoplasmic boundaries as two separate but consecutive steps. Moreover, the proposed DCAC model collects information from the H- and E-channel images to efficiently control the contour's movement towards the cytoplasmic boundary. The two channel images provide information to compute the external energy force required to efficiently differentiate MK cytoplasmic regions from other tissue constituents. This helps to control the contour's expansion and prevent over-segmentation.

## IV. CONCLUSIONS

In this paper, we presented a framework to delineate megakaryocytes (MKs) in bone marrow trephine histology images. The framework first delineates MK nuclei by using color and texture features in a supervised machine learning approach. To delineate MK cytoplasm, the framework uses a novel dual-channel active contour (DCAC) model that employs the previously delineated nuclear boundary as the initial contour, as well as intensity features of the constituent stain channel images. Specifically, our proposed DCAC model employs the Hematoxylin and Eosin channel images to efficiently determine the extent of MK cytoplasm under the observation that the cytoplasm is usually surrounded by non-smooth regions. The DCAC model also uses a ring-like region to restrict the contour's evolution and prevent over-segmentation. Experimental results show that the proposed framework can accurately delineate both MK nuclei and cytoplasm, providing more accurate results with low variability and computational time than those obtained by recent methods. We showed that our DCAC model is particularly successful in delineating MK cytoplasmic boundaries delimited by weak edges and partially occluded by nearby cells or other non-MK cytoplasmic regions. In further research, we will concentrate on using the output of our proposed framework to assist hematopathologists to analyze and subgroup the MPNs.

## REFERENCES

- [1] G. J. Titmarsh *et al.*, "How common are myeloproliferative neoplasms? a systematic review and meta-analysis," *Am J Hematol.*, vol. 89, no. 6, pp. 581–587, 2014.
- [2] B. J. Bain *et al.*, *Bone marrow pathology*, 4th ed. West Sussex, UK: Blackwell Science Ltd., 2010.

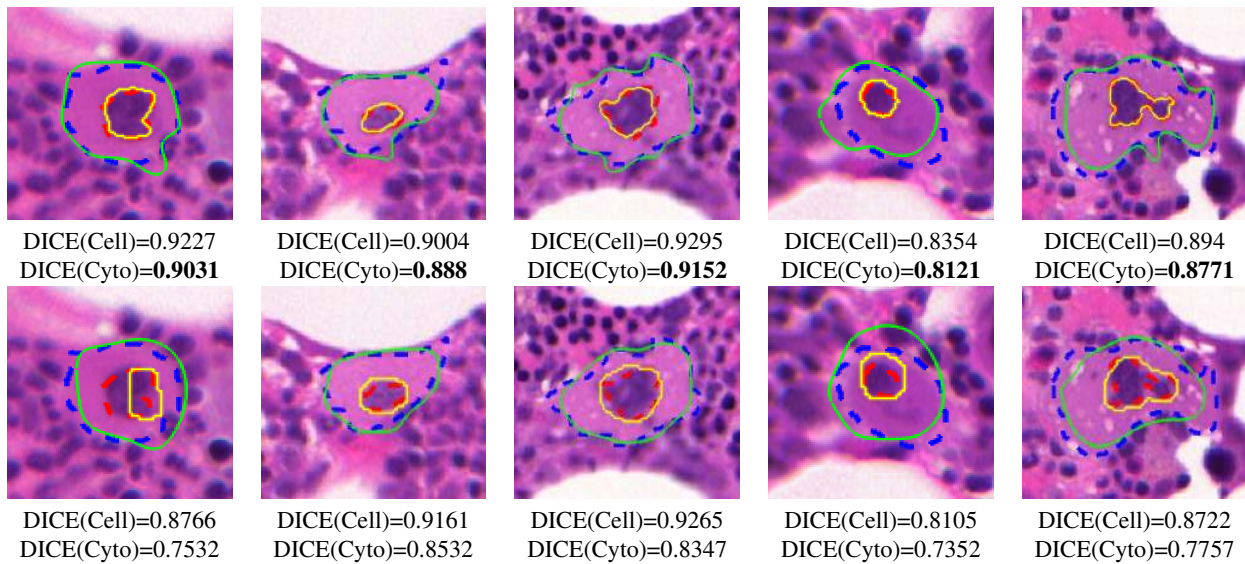


Fig. 10. Visual results of our entire proposed framework (upper row) and the multi-region active contour model (bottom row) for delineation of MK nuclear and cytoplasmic boundaries. Yellow contours denote the identified nuclear boundaries; green contours denote the identified cytoplasmic boundaries; red and blue dashed contours denote the ground truth of nuclear and cytoplasmic boundaries, respectively.

- [3] A. A. Fauser and H. A. Messner, "Identification of megakaryocytes, macrophages, and eosinophils in colonies of human bone marrow containing neutrophilic granulocytes and erythroblasts," *Blood*, vol. 53, no. 5, pp. 1023–1027, 1979.
- [4] J. W. Vardiman *et al.*, "The 2008 revision of the world health organization (WHO) classification of myeloid neoplasms and acute leukemia: rationale and important changes," *Blood*, vol. 114, no. 5, pp. 937–951, 2009.
- [5] B. S. Wilkins *et al.*, "Bone marrow pathology in essential thrombocythemia: interobserver reliability and utility for identifying disease subtypes," *Blood*, vol. 111, no. 1, pp. 60–70, 2008.
- [6] T. Barbui *et al.*, "Problems and pitfalls regarding who-defined diagnosis of early/prefibrotic primary myelofibrosis versus essential thrombocythemia," *Leukemia*, vol. 27, no. 10, pp. 1953–1958, 2013.
- [7] J. Thiele *et al.*, "Early stage idiopathic (primary) myelofibrosis - current issues of diagnostic features," *Leukemia & lymphoma*, vol. 43, no. 5, pp. 1035–1041, 2002.
- [8] M. N. Gurcan *et al.*, "Histopathological image analysis: A review," *IEEE reviews in biomedical engineering*, vol. 2, pp. 147–171, 2009.
- [9] M. Veta *et al.*, "Breast cancer histopathology image analysis: A review," *IEEE Trans. Biomed. Eng.*, vol. 61, no. 5, pp. 1400–1411, 2014.
- [10] H. Irshad *et al.*, "Methods for nuclei detection, segmentation and classification in digital histopathology: A review. current status and future potential," *IEEE review in biomedical engineering*, vol. 7, pp. 97–114, 2014.
- [11] E. Cosatto *et al.*, "Grading nuclear pleomorphism on histological micrographs," in *Pattern Recognition, 2008. ICPR 2008. 19th International Conference on*, 2008, pp. 1–4.
- [12] A. Mouelhi *et al.*, "Automatic segmentation of clustered breast cancer cells using watershed and concave vertex graph," in *Communications, Computing and Control Applications (CCCA), 2011 International Conference on*, 2011, pp. 1–6.
- [13] A. Veillard *et al.*, "Cell nuclei extraction from breast cancer histopathology images using color, texture, scale and shape information," *Diagnostic Pathology*, vol. 8, no. 1, p. S5, 2013.
- [14] J. P. Vink *et al.*, "Efficient nucleus detector in histopathology images," *Journal of microscopy*, vol. 249, no. 2, pp. 124–135, 2013.
- [15] H. Fatakdawala *et al.*, "Expectation maximization driven geodesic active contour with overlap resolution (emagacor): Application to lymphocyte segmentation on breast cancer histopathology," *IEEE Trans. Biomed. Eng.*, vol. 57, no. 7, pp. 1676–1689, 2010.
- [16] F. Bunyak *et al.*, "Histopathology tissue segmentation by combining fuzzy clustering with multiphase vector level sets," in *Software tools and algorithms for biological systems*, 2011, pp. 413–424.
- [17] X. Qi *et al.*, "GPU enabled parallel touching cell segmentation using mean shift based seed detection and repulsive level set," in *Medical Image Computing, Computer Assisted Intervention*, 2010, pp. 30–40.
- [18] A. Hafiane *et al.*, "Clustering initiated multiphase active contours and robust separation of nuclei groups for tissue segmentation," in *Pattern Recognition, 2008. ICPR 2008. 19th International Conference on*, 2008, pp. 1–4.
- [19] J. Xu *et al.*, "Markov random field driven region-based active contour model (MaRACel): application to medical image segmentation," in *International Conference on Medical Image Computing and Computer-Assisted Intervention*, 2010, pp. 197–204.
- [20] T. F. Chan and L. A. Vese, "Active contours without edges," *IEEE Trans. Image Process.*, vol. 10, no. 2, pp. 266–277, 2001.
- [21] L. A. Vese and T. F. Chan, "A multiphase level set framework for image segmentation using the mumford and shah model," *International journal of computer vision*, vol. 50, no. 3, pp. 271–293, 2002.
- [22] A. Tsai *et al.*, "Curve evolution implementation of the mumford-shah functional for image segmentation, denoising, interpolation, and magnification," *IEEE Trans. Image Process.*, vol. 10, no. 8, pp. 1169–1186, 2001.
- [23] N. Paragios and R. Deriche, "Geodesic active regions and level set methods for supervised texture segmentation," *International Journal of Computer Vision*, vol. 46, no. 3, pp. 223–247, 2002.
- [24] S. Gao and T. D. Bui, "Image segmentation and selective smoothing by using mumford-shah model," *IEEE Trans. Image Process.*, vol. 14, no. 10, pp. 1537–1549, 2005.
- [25] J. E. Solem *et al.*, "Initialization techniques for segmentation with the chan-vese model," in *Pattern Recognition, 2006. ICPR 2006. 18th International Conference on*, vol. 2, 2006, pp. 171–174.
- [26] R. Xia *et al.*, "An optimal initialization technique for improving the segmentation performance of chan-vese model," in *Automation and Logistics, 2007 IEEE International Conference on*, 2007, pp. 411–415.
- [27] Y. Shi and W. C. Karl, "A fast level set method without solving PDEs," in *Acoustics, Speech, and Signal Processing, 2005. Proceedings.(ICASSP'05). IEEE International Conference on*, vol. 2, 2005, pp. 97–100.
- [28] Y. Pan *et al.*, "Efficient implementation of the chan-vese models without solving PDEs," in *Multimedia Signal Processing, 2006 IEEE 8th Workshop on*, 2006, pp. 350–354.
- [29] C. Li *et al.*, "Level set formulation without re-initialization: a new variational formulation," in *CVPR 2005. IEEE Computer Society Conference on*, vol. 1, 2005, pp. 430–436.
- [30] L. Pi *et al.*, "A variational formulation for segmenting desired objects in color images," *Image and Vision Computing*, vol. 25, no. 9, pp. 1414–1421, 2007.
- [31] C. Li *et al.*, "Implicit active contours driven by local binary fitting energy," in *CVPR 2007. IEEE Conference on*, 2007, pp. 1–7.
- [32] X. F. Wang *et al.*, "An efficient local chan-vese model for image segmentation," *Pattern Recognition*, vol. 43, no. 3, pp. 603–618, 2010.

- [33] Y. Zhou *et al.*, "Active contours driven by localizing region and edge-based intensity fitting energy with application to segmentation of the left ventricle in cardiac ct image," *Neurocomputing*, vol. 156, pp. 199–210, 2015.
- [34] Z. Ji *et al.*, "Active contour driven by local likelihood image fitting energy for image segmentation," *Information Science*, vol. 301, pp. 285–304, 2015.
- [35] M. Shen and Y. Wu, "A new improved local chan-veye model," in *SPIE 9443, Sixth International Conference on Graphic and Image Processing(ICGIP 2014)*, 2015.
- [36] E. S. Brown *et al.*, "Completely convex formulation of the chan-veye image segmentation model," *International journal of computer vision*, vol. 98, no. 1, pp. 103–121, 2012.
- [37] G. Liu *et al.*, "Gradient descent with adaptive momentum for active contour models," *IET Computer Vision*, vol. 8, no. 4, pp. 287–298, 2014.
- [38] J. Spencer and K. Chen, "Stabilised bias field: segmentation with intensity inhomogeneity," *Journal of Algorithms & Computational Technology*, vol. 10, no. 4, pp. 302–313, 2016.
- [39] P. W. Huang and Y. H. Lai, "Effective segmentation and classification for HCC biopsy images," *Pattern Recognition*, vol. 43, no. 4, pp. 1550–1563, 2010.
- [40] S. Ali *et al.*, "Selective invocation of shape priors for deformable segmentation and morphologic classification of prostate cancer tissue microarrays," *Computerized medical imaging and graphics*, vol. 41, pp. 3–13, 2015.
- [41] M. S. Nosrati and G. Hamarneh, "Local optimization based segmentation of spatially-recurring, multi-region objects with part configuration constraints," *IEEE Trans. Med. Imag.*, vol. 33, no. 9, pp. 1845–1859, 2014.
- [42] B. Ballaro *et al.*, "An automated image analysis methodology for classifying megakaryocytes in chronic myeloproliferative disorders," *Medical Image Analysis*, vol. 12, pp. 703–712, 2008.
- [43] V. Franco *et al.*, "Megakaryocytic features useful for the diagnosis of myeloproliferative disorders can be obtained by a novel unsupervised software analysis," *Histology and Histopathology*, vol. 21, no. 8, pp. 813–821, 2006.
- [44] T. H. Song *et al.*, "A circumscribing active contour model for delineation of nuclei and membranes of megakaryocytes in bone marrow trephine biopsy images," in *SPIE 9420, Medical Imaging 2015: Digital Pathology*, 2015.
- [45] A. M. Khan *et al.*, "A non-linear mapping approach to stain normalization in digital histopathology images using image-specific colour deconvolution," *IEEE Trans. Biomed. Eng.*, vol. 61, pp. 1729–1738, 2014.
- [46] J. Bruna and S. Mallat, "Invariant scattering convolution network," *IEEE Trans. Pattern Anal. Mach. Intell.*, vol. 35, no. 8, pp. 1872–1886, 2013.
- [47] C. D. Boor, *A practical guide to splines*. New York: Springer-Verlag, 1978.
- [48] J. Mille, "Narrow band region-based active contours and surfaces for 2D and 3D segmentation," *Computer Vision and Image Understanding*, vol. 113, no. 9, pp. 946–965, 2009.
- [49] Q. Zheng and E. Q. Dong, "Narrow band active contour model for local segmentation of medical and texture images," *Acta Automatica Sinica*, vol. 39, no. 1, pp. 21–30, 2013.
- [50] A. Khadidos *et al.*, "Weighted level set evolution based on local edge features for medical image segmentation," *IEEE Trans. Image Process.*, 2017.